Friction

Research Article

Development of a machine learning-based surrogate model for friction prediction in textured journal bearings

Yujun Wang✉, Georg Jacobs, Shuo Zhang, Benjamin Klinghart, Florian König

Cite this article: Wang YJ, Jacobs G, Zhang S, et al. *Friction* 2025, **13**(8): 9441051. https://doi.org/10.26599/FRICT.2025.9441051

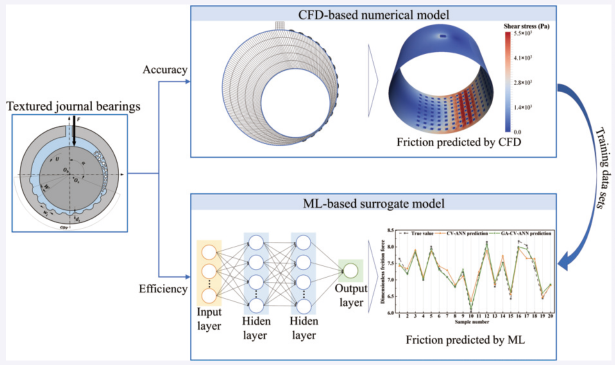

ABSTRACT: Surface textures in journal bearings offer significant potential for reducing friction and enhancing energy efficiency. However, the complexity of texture configurations necessitates an accurate and efficient performance prediction model to properly design textured journal bearings. To address this issue, this study develops a machine learning (ML)-based surrogate model to predict friction in textured journal bearings. First, computational fluid dynamics (CFD) models employing a dynamic mesh algorithm are developed to generate accurate data sets. Furthermore, three ML methods are trained and compared to select the most suitable prediction method: artificial neural network (ANN), support vector regression (SVR), and Gaussian process regression (GPR). Among these ML methods, ANN shows the best prediction performance. Given the high computational cost of CFD simulations, the prediction accuracy of the ANN-based surrogate model is further enhanced without the need for additional data sets. This enhancement is achieved through an architecture design based on cross-validation and further optimization utilizing the genetic algorithm. Eventually, the average prediction accuracy is improved to 98.81% from 95.89%, with the maximum error reduced to 3.25% from 13.17%. These findings demonstrate the potential of ML in the performance prediction in textured journal bearings and provide a promising approach for broader applications in developing highly efficient and accurate ML-based surrogate models, particularly in cases with limited available training data sets.

KEYWORDS: journal bearings; surface textures; friction; machine learning; computational fluid dynamics (CFD)

1 Introduction

With the increase in energy prices and environmental requirements, the demand for energy efficiency and sustainability is growing [1, 2]. Approximately 20% of the world total energy consumption is used to overcome friction, which is recognized as the main cause in the energy cost [3, 4]. Therefore, growing attention has been given on the improvement of tribological performance by the reduction of friction [5, 6]. In this context, surface textures have been demonstrated to be a promising way to reduce friction by numerous theoretical and experimental studies [7–10]. Several beneficial effects of surface textures in terms of friction have been identified. Surface textures can act as lubricant reservoirs and reduce the contact area [11–13]. Moreover, textures can build up an additional micro-hydrodynamic pressure, which contributes to an increase in load-carrying capacity [14–16].

The effects of textures on the tribological performance of journal bearings have been studied over years. The studies encompass two aspects: their effects under various texture geometries and distributions, as well as under various operating conditions [17]. Regarding the texture geometries and distributions, Tala-Ighil et al. [18] studied the influence of texture size and distribution on the bearing characteristics. The results indicated that the effect of texture size on the bearing performance was influenced by the texture distribution. Dobrica et al. [19] pointed out that the texture distribution covering the full circumference of the bearing surface resulted in a worse lubrication performance compared with the non-textured bearings. This finding was confirmed later by Tala-Ighil et al. [20] and Khatri and Sharma [21]. Afterwards, the effects of the texture depth and texture distribution covering the partial circumference of the bearing surface were investigated by Liang et al. [22]. They found that shallow textures were better for the convergent area, while deep textures were better for the divergent area.

In addition to the interaction between texture geometries and distributions, textured journal bearings also exhibit considerably different performance under various operating conditions. Brizmer and Kligerman [23] reported that the beneficial influence of partial texturing was quite appreciable at low eccentricity ratios, which corresponded to the low-load or high-speed operating

Institute for Machine Elements and Systems Engineering, RWTH Aachen University, Aachen 52062, Germany.

✉ Corresponding author. E-mail: yujun.wang@imse.rwth-aachen.de

Received: September 6, 2024; Revised: November 8, 2024; Accepted: December 1, 2024

conditions. While with the increasing eccentricity ratios, the beneficial effect was weakening. According to Cupillard et al. [24, 25], the optimum texture depth and the relative texture extension in the circumferential direction were highly influenced by the eccentricity of journal bearings. Similar conclusions were made by Lin et al. [26] and Marian et al. [27], showing that the optimum distribution of textures strongly depended on the operating conditions of the journal bearing system. Singh and Awasthi [28] also found that the effect of texture distribution on the bearing performance was dependent on the bearing eccentricity. The aforementioned findings reveal that, the design of surface texture patterns in journal bearings involves numerous parameters, and the relationships between these parameters and bearing performance exhibit nonlinear behaviour. At the same time, the correlations between textures and bearing performance are affected by the interactions among texture parameters. These complexities present a significant challenge for accurately predicting the performance of textured journal bearings, making traditional parametric studies not effective enough.

Machine learning (ML) algorithms offer the possibility of predicting complex relationships in a more efficient way, thereby drawing growing attention in the field of tribology [29, 30]. This method has been successfully utilized in the performance prediction of journal bearings. Moschopoulos et al. [31] developed a ML procedure to predict the loading condition based on the sound and vibration data. Hess and Shang [32] presented an artificial neural network (ANN) model to approximate the pressure distribution of a journal bearing working under the elasto-hydrodynamic lubrication (EHL) regime. A support vector regression (SVR) model was developed by Roy and Dey to predict the steady-state and dynamic characteristics of hydrodynamic journal bearings [33]. Baş and Karabacak [34] compared three different ML methods for the friction prediction of radial journal bearings, including ANN, SVR, and regression trees. In addition to the applications in journal bearings, ML has also shown its potentials in textured contacts. Otero et al. [35] developed an ANN model to predict the friction coefficient of the textured surface in a ball-on-disc contact. Marian et al. [36] applied Gaussian process regression (GPR) and linear regression methods to qualitatively feature the influence of micro-textures in a single EHL contact, which was a tribological approximation model of rolling bearings. Li et al. [37] compared five ML algorithms for predicting the friction coefficient of sliding friction pairs with textures. However, from the references, the studies in which ML techniques are applied to the performance prediction of textured journal bearings are still new.

The accuracy of an ML-based surrogate model is highly dependent on the accuracy of training data [38, 39]. Therefore, the accurate training data should be provided for the performance prediction of textured journal bearings. However, the classical Reynolds equation neglects the inertia effect and the flow across the film gap when simplified from the Navier–Stokes (N–S) equations [40]. Due to this, the texture-induced microflow effects, including the inertia effect and vortices within textures, cannot be considered by Reynolds equation [41–43]. Arghir et al. [41] reported that a positive load-carrying capacity could be generated by the inertia effect in textures, especially under lubrication conditions with a high Reynolds number. In addition, the vortices were found within textures by Sahlin et al. [43], and were indicated to have a considerable effect on the textured bearing performance [14, 44–46]. Consequently, a computational fluid dynamics (CFD) model based the N–S equations is required to prepare the training data sets, which can consider the texture-induced microflow effects and the macro-hydrodynamic lubricating film formation at the same time [47]. Nevertheless, this approach compromises computational efficiency, as the dramatic increase in mesh cell numbers is required to capture the texture-induced microflow [5]. In addition, the multiple design parameters of textures mean that a large amount of training data is required, which further leads to increased time requirements. Therefore, in order to reduce the high computational cost, and improve the prediction efficiency, it is crucial to explore methods that can improve prediction accuracy without the need for additional data sets.

To summarize, it is critical to develop a highly efficient and accurate ML-based surrogate model for the friction prediction of textured journal bearings. For this purpose, CFD models of textured journal bearings are first built to prepare accurate data sets for the ML-based surrogate model. Subsequently, using identical data sets, three different ML methods, including ANN, SVR, and GPR, are employed and compared to determine the most suitable algorithm for predicting the friction of textured journal bearings. Furthermore, the architecture design through cross-validation and further optimization through the genetic algorithm are conducted, aiming for a higher prediction accuracy based on identical data sets. This work demonstrates the potential of ML algorithms in efficiently predicting the friction performance of textured journal bearings with varying operating conditions and texture parameters. In addition, the proposed optimization strategy highlights the potential to reduce the size of the data sets required to train an accurate and efficient ML-based surrogate model.

2 Numerical models

2.1 Textured journal bearing model

The textured journal bearing in the current study is schematically depicted in Fig. 1. The smooth shaft rotates in an anti-clockwise direction. The partially textured bearing stays stationary. The utilized parameters of the textured journal bearing are listed on the left side of Table 1. The determination of the texture parameters is based on previous works in Refs. [19, 20, 46, 48]. The oil is pumped into the bearing from the upper inlet hole with the inlet pressure (p_{in}) and flows out from both sides with the ambient pressure (p_{out}). The external load (F) is applied vertically on the shaft. The boundary conditions and lubricant properties are listed on the right side of Table 1.

2.2 Governing equations

2.2.1 Governing equations of the flow field

When simulating the lubrication performance of textured journal bearings, the accuracy depends on the ability to accurately capture the flow behaviour of the lubricant. One important flow behaviour is the so-called cavitation effect, which happens when the pressure falls below the saturation pressure (p_{sat}) [49]. Consequently, in this work, the *cavitatingFoam* solver in OpenFOAM is used for the cavitating flow. This solver is based on the homogeneous equilibrium model, which assumes the mixture of liquid and vapor to be in a mechanical and thermodynamic equilibrium [42]. Besides, the compressibility of the mixture flow is considered in the simulations. Therefore, the cavitation model is based on the relations of the pressure and density as a closure equation [50, 51]. Combined with the cavitation model, the N–S equations, which are derived from mass conservation and momentum conservation, are used to solve the fluid flow [52]. Details about

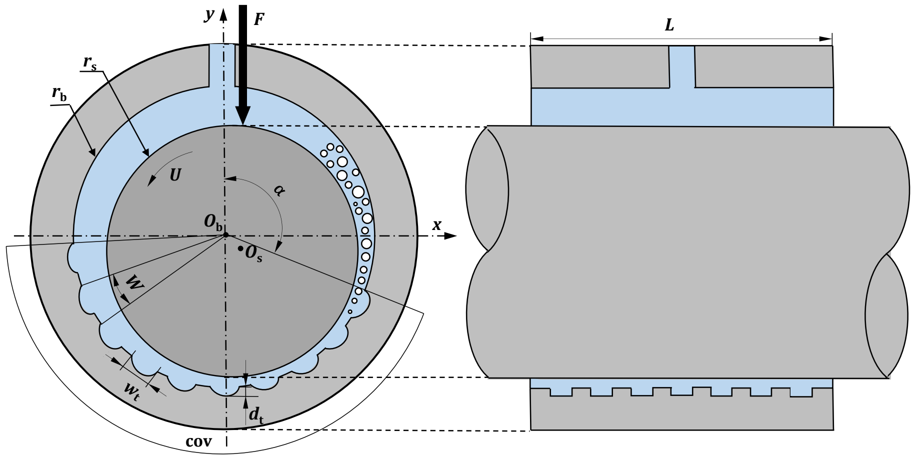

Fig. 1 Schematic representation of a hydrodynamic textured journal bearing.

Table 1 Parameters used in this study, left side: geometry parameters of the textured journal bearing; right side: operating conditions and lubricant properties

Bearing and texture parameter	Value	Operating and lubricant parameter	Value
Bearing radius, r_b (mm)	15	Rotational speed, U (r·min^{-1})	1,000
Bearing width, L (mm)	20	Inlet pressure, p_{in} (Pa)	300,000
Shaft radius, r_s (mm)	14.97	Outlet pressure, p_{out} (Pa)	101,325
Clearance $C = r_b - r_s$ (mm)	0.03	Saturation pressure, p_{sat} (Pa)	29,185
Starting angle of texture zone, α (°)	5–180	Density of oil, ρ_l (kg·m^{-3})	822
*Co*verage of texture zone, cov (°)	0–170	Dynamic viscosity of oil, η_l (Pa·s)	0.014
Texture width ratio, w_t/W	0.2–0.96	Density of vapor, ρ_v (kg·m^{-3})	1.29
Texture depth ratio, d_t/C	0–3	Dynamic viscosity of vapor, η_v (Pa·s)	5.953×10^{-6}

the cavitation model and the N–S equations can be found in the Appendix.

By solving the N–S equations, the shear stress field within a journal bearing can be predicted. Then, the dimensionless friction force f_d is calculated by the integration the wall shear stress over the nominal contact area between the shaft and journal bearing [53]:

$$f_d = \frac{C}{\eta_l \omega r_s^2 L} \iint_A \overline{\tau} \mathrm{d}A \tag{1}$$

where C means the clearance; η_l is the viscosity of oil; ω represents the angular speed of the shaft; L is the width of the bearing (Fig. 1); $\overline{\tau}$ is the shear stress term; A is the nominal contact area between the shaft and journal bearing.

2.2.2 Load balance equations and dynamic mesh algorithm

Excepting the shear stress, the hydrodynamic pressure distribution of textured journal bearings can also be predicted by solving the N–S equations. Then, the hydrodynamic load-carrying capacity (F_h^t) at time step t can be calculated as

$$F_h^t = \sqrt{(F_{hx}^t)^2 + (F_{hy}^t)^2}$$
$$\begin{cases} F_{hx}^t = r_s \int_0^L \int_0^{2\pi} p^t \sin\theta \mathrm{d}\theta \mathrm{d}z \\ F_{hy}^t = r_s \int_0^L \int_0^{2\pi} p^t \cos\theta \mathrm{d}\theta \mathrm{d}z \end{cases} \tag{2}$$

where F_{hx}^t and F_{hy}^t are the hydrodynamic load-carrying capacities in x and y directions at time step t, which are integrated from the hydrodynamic pressure (p^t) at time step t.

If F_h^t cannot achieve balance with the external load (F) within this time step, the shaft will move. As a result, this movement changes the simulation domain. Consequently, the mesh in the simulation domain needs to be updated during the simulation. To determine the equilibrium position under the specified operating condition, a dynamic mesh algorithm based on the load balance equations is proposed in the present study. This model can be employed for both untextured and textured journal bearings. The steps for updating the mesh are as follows.

Step 1: Calculation of the displacement of the shaft

In this step, the acceleration of the shaft is first calculated by the load imbalance as Eq. (3):

$$\begin{cases} a_x^t = \dfrac{F_{hx}^t - F_x}{m} \\ a_y^t = \dfrac{F_{hy}^t - F_y}{m} \end{cases} \tag{3}$$

where a_x^t and a_y^t are the accelerations of the shaft in x and y directions at time step t, respectively; m is the mass of shaft; F_x and F_y are the applied loads in x and y directions, respectively. In this study, since the external load is applied vertically on the shaft, F_x is set to 0, and F_y is equivalent to F, as shown in Fig. 1.

After that, the motion speed and the displacement of the shaft are calculated as Eq. (4):

$$\begin{cases} V_x^t = V_x^{t-\Delta t} + a_x^t \cdot \Delta t \\ V_y^t = V_y^{t-\Delta t} + a_y^t \cdot \Delta t \end{cases} \tag{4}$$

$$\begin{cases} \Delta \widehat{x}^t = V_x^t \cdot \Delta t \\ \Delta \widehat{y}^t = V_y^t \cdot \Delta t \end{cases} \tag{5}$$

where V_x and V_y are the motion speeds of the shaft in x and y directions, respectively; $\Delta \widehat{x}^t$ and $\Delta \widehat{y}^t$ are the displacements of the shaft in these two directions, respectively. In this work, $V_x^{\,0}$ and $V_y^{\,0}$ are set to be zero to start the simulation.

Step 2: Determination of the mesh updating domain

To increase the simulation efficiency, the mesh updating domain needs to be determined. In this work, the entire mesh domain is divided into two sub-domains: oil film gap domain and texture domain, see Eq. (6).

$$\begin{cases} n_j \leq n_{\text{total}}, & \text{oil film gap domain} \\ n_j > n_{\text{total}}, & \text{texture domain} \end{cases} \tag{6}$$

where n_j is the radial reticulate layer for each mesh node j; n_{total} is the total number of radial reticulate layers in the oil film gap domain ($n_{\text{total}} = 5$ in Fig. 2).

The oil film gap domain refers to the area between the two blue lines in Fig. 2(a). The shaft is moving with an unbalanced load. Therefore, the nodes within the oil film gap domain should be updated. In contrast, the nodes within the texture domain are not updated, because the textured bearing wall is considered to be stationary in the present work.

Step 3: Calculation of the updated mesh node position

In this step, the coordinates $(\widehat{x}_j^t, \widehat{y}_j^t)$ of each node j within the oil film gap domain at the time step t are calculated based on their radial reticulate layer n_j using Eq. (7):

$$\begin{cases} \widehat{x}_j^t = \widehat{x}_j^{t-\Delta t} + \left(1 - \dfrac{n_j}{n_{\text{total}}}\right) \Delta \widehat{x}^t \\ \widehat{y}_j^t = \widehat{y}_j^{t-\Delta t} + \left(1 - \dfrac{n_j}{n_{\text{total}}}\right) \Delta \widehat{y}^t \end{cases} \tag{7}$$

After all the above procedures, the mesh update at time step t is finished.

To clearly show the capability of this dynamic mesh algorithm, Fig. 2 illustrates the mesh distribution of a textured journal bearing with an exaggerated clearance. As shown in Fig. 2(a), the above-mentioned dynamic mesh algorithm is based on the structured mesh distribution. It can be observed from Fig. 2(b) that the updated mesh can keep a structured distribution even at a large eccentricity ratio. The comparison of mesh parameters is exemplarily listed in Table 2. After the mesh update, the mesh cells and points remain the same as in the initial mesh. Additionally, skewness and aspect ratio are commonly employed to quantify the mesh quality [54]. High values of skewness or aspect ratio may impair the accuracy of results and reduce the convergence speed. The threshold for skewness and aspect ratio in OpenFOAM is 4 and 1,000, respectively [54]. Consequently, as indicated in Table 2, the dynamic mesh algorithm in the present study can keep a satisfied mesh quality during simulation.

Therefore, the whole flowchart of the simulation is presented in Fig. 3. The pressure–velocity coupling equations are solved by the GAMG matrix solver with DICGaussSeidel smoother [52]. The tolerances are set as 10^{-6}. A relaxation factor for pressure between two timesteps is set to increase the model stability, with the value of 0.1. When $F_{\text{error}} = |F_{\text{h}}^t - F| / F < 10^{-3}$, the simulation will be stopped.

2.3 Validation

Gupta et al. [55] measured the pressure on the middle circumference of a textured journal bearing. To verify the accuracy of the present model, validation is carried out with the same structural parameters and operating conditions as in the experiments. The validation is conducted under four operating conditions, with rotational speeds of 1,000 and 2,000 r·min^{-1} at varying loads of 600 and 800 N. The maximum pressure values for the four cases are compared with experimental results, as shown in Fig. 4. A good agreement with the experimental results can be found and all the absolute errors are below 8.1%. Considering the potential tolerances in manufacturing, assembling, and measuring, it can be concluded that the numerical results are within an acceptable range. Therefore, it is sufficient to show the feasibility and accuracy of the current CFD model in providing data sets for the ML-based surrogate model.

2.4 Influence of surface textures on friction—an exemplary study

Based on the validated model, the influence of textures on the friction performance of journal bearings is exemplarily shown in this section. The structural parameters for the textured journal bearing are as follows: texture width ratio w_t/W = 0.4, texture

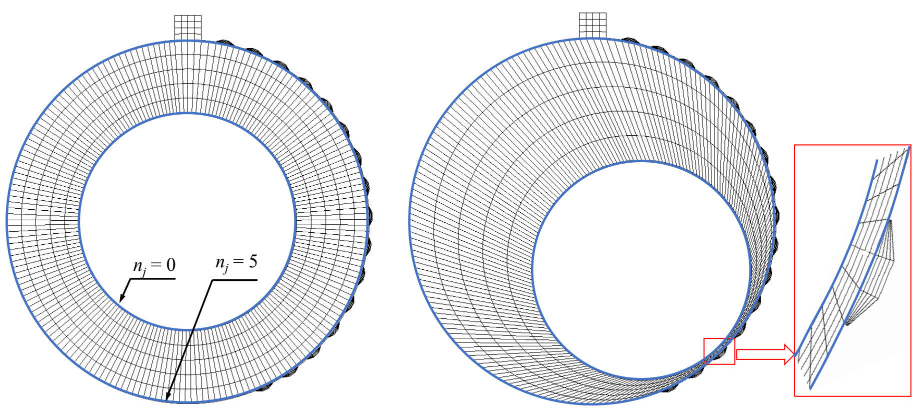

(a) Initial mesh

(b) Updated mesh based on the dynamic mesh algorithm

Fig. 2 Mesh distribution of a textured journal bearing with an exaggerated clearance ($n_{\text{total}} = 5$).

Table 2 Comparison of mesh parameters for initial and updated meshes

Item	Cells	Points	Average skewness	Average aspect ratio
Initial mesh	649,984	787,119	0.015	22.80
Updated mesh	649,984	787,119	0.021	32.00

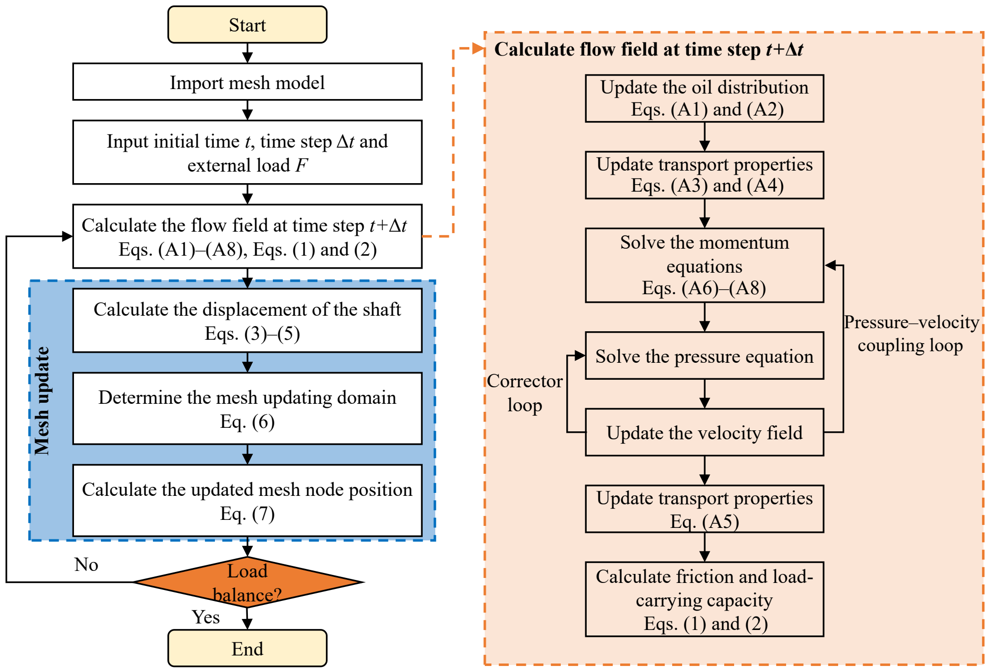

Fig. 3 Simulation flowchart, including the calculation of flow field and the dynamic mesh algorithm.

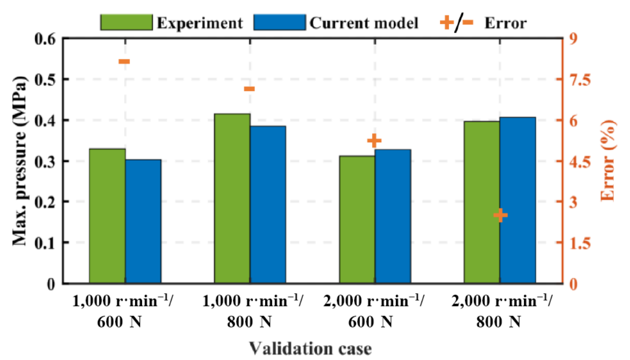

Fig. 4 Comparison of experimental (green) and simulation (blue) results ("+" indicates positive error; "–" indicates negative error).

depth ratio $d_t/C = 0.5$, starting angle $\alpha = 72°$, and texture coverage cov = 137.5°. The operating conditions for both non-textured and textured bearings are the same, with a rotational speed of 1,000 r·min^{-1} and an external load of 416 N.

The pressure distributions of non-textured and textured journal bearings are shown in Fig. 5. A quantitative comparison of the pressure distribution along the centerline of the bearing is provided in Fig. 5(c). The presence of textures induces the micro-hydrodynamic pressure as the lubricant flows through them, which can lead to an increase in load-carrying capacity. This finding aligns with the outcomes published in Refs. [19, 27]. However, as shown in Fig. 5(b), when textures are distributed within the high-pressure region, they can cause a disruption to this region, which is the primary load-carrying area of the bearing. This disruption leads to a decrease in the load-carrying capacity, thereby reducing the minimum oil film thickness. In this case, the minimum film thickness of the textured bearing is decreased by 2.54% compared with the non-textured bearing, as shown in Table 3.

The effects of textures on the wall shear stress are shown in Fig. 6. The variation in wall shear stress is closely related to the film thickness. On one hand, the reduction in the minimum film thickness of the textured bearing results in an increase in the maximum value of the wall shear stress. The increased wall shear stress in the textured bearing can be observed from the comparison of the wall shear stress distribution in Fig. 6(c). As the friction is the integral of the wall shear stress, this increase will lead to the increase in friction. On the other hand, the local increase in film thickness at textures leads to a significant reduction in the wall shear stress. This helps to reduce the friction [10, 14]. Therefore, the impact of textures on the friction force of the journal bearing depends on the trade-off between these two aspects. In this case, although the wall shear stress increases locally, the overall friction is reduced by textures. The friction force of the textured bearing is 8.76% lower than that of the non-textured bearing. A detailed comparison of the above performance parameters for the two types of bearings is presented in Table 3.

3 Machine learning-based surrogate model

From the aforementioned exemplary study, it can be concluded that textures have a significant impact on the friction performance of journal bearings. The friction performance of textured journal bearings is considerably influenced by the texture geometry and distribution parameters, as well as the operating conditions [20, 56]. Therefore, the friction prediction of textured journal bearings requires to consider both texture parameters and operating parameters. To achieve the efficient prediction, the ML-based surrogate model is developed in this section.

3.1 Input and output parameters

The ML-based surrogate model is trained for a wide range of texture parameters and operating parameters. The input parameters include texture geometry parameters (texture width ratio, w_t/W; texture depth ratio, d_t/C), texture distribution parameters (starting angle of texture zone, α; coverage of texture zone, cov), as well as external load F. The output parameter is the dimensionless friction force of textured journal bearings f_d. The design range of each input parameter is shown in Table 4.

The datasets are generated using the Latin hypercube sample function in MATLAB. Therefore, all the design points are randomly distributed within the design range for each input

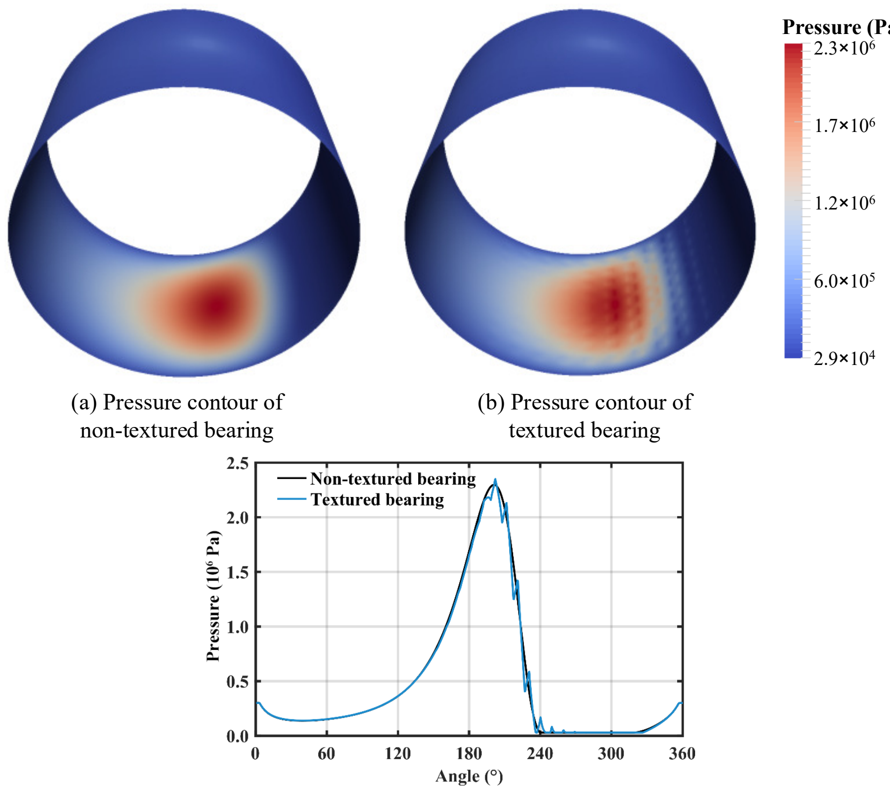

(a) Pressure contour of non-textured bearing

(b) Pressure contour of textured bearing

(c) Pressure profiles along the center plane of non-textured and textured bearings

Fig. 5 Comparison of pressure distributions of non-textured and textured bearings.

Table 3 Comparison of performance parameters for non-textured and textured bearings

	Minimum film thickness (μm)	Maximum pressure (Pa)	Maximum wall shear stress (Pa)	Dimensionless friction force
Non-textured bearing	7.86	2,296,224	5,001.63	8.45
Textured bearing	7.66	2,371,173	6,712.21	7.71
Difference (%)	−2.54	3.26	34.20	−8.76

parameter. 170 design points with different input parameter combinations are executed with the validated CFD model. The input design points and the corresponding dimensionless friction forces are stored as data sets (6 × 170 MATLAB structure array). Among these 170 sets of data, 150 sets of data are used to train ML models. The remaining 20 sets of data are used to evaluate the prediction accuracy of the trained surrogate model.

To ensure stable and efficient training, the normalization is applied to both input and output parameters using the standardised min-max normalization function, that reads

$$\widehat{z} = \frac{z - z_{\min}}{z_{\max} - z_{\min}}\left(q_{\text{upper}} - q_{\text{lower}}\right) + q_{\text{lower}} \tag{8}$$

where $\widehat{z}$ is the final normalized value; z represents the original value of the data point; $z_{\min}$ and $z_{\max}$ denote the minimum and maximum values in the original data sets, respectively; q_{lower} and q_{upper} are the lower and upper normalized unit values, which are 0 and 1 in this study, respectively.

3.2 Machine learning methods

To determine the most appropriate prediction algorithm for textured journal bearings, three different ML methods are employed and compared using identical data sets. The three methods include ANN, SVR, and GPR, which are three commonly used ML methods for prediction [29].

3.2.1 *Artificial neural network*

ANN is an ML model composed of interconnected nodes, designed to mimic the functioning of biological neurons [57]. The training data flow from the input layer through the hidden layers to produce an output. Each connection between nodes is determined by the weights and biases. By applying activation functions, the network can capture complex relationships within the data. There are three popular activation functions for the hidden layer, including the hyperbolic tangent sigmoid function (tanh), the logistic sigmoid function (Sigmoid), and the rectified linear function (ReLU). Usually, the pure linear function (purelin) is used for the activation function of the output layer [57, 58].

As the initial design, 1 hidden layer with 5 neurons is chosen. The remaining parameters are set to the default values provided by MATLAB as initial choices. To avoid the unnecessary computational overhead or overfitting, the training stops when any of the following conditions are met: reaching the maximum number of epochs (1,000), achieving the target minimum error (10^{-4}), encountering the maximum number of consecutive failures (6), or reaching the target gradient descent value (10^{-6}). The design parameters for the initial ANN model are shown in Table 5.

3.2.2 *Support vector regression*

SVR is a ML algorithm that extends the concept of support vector

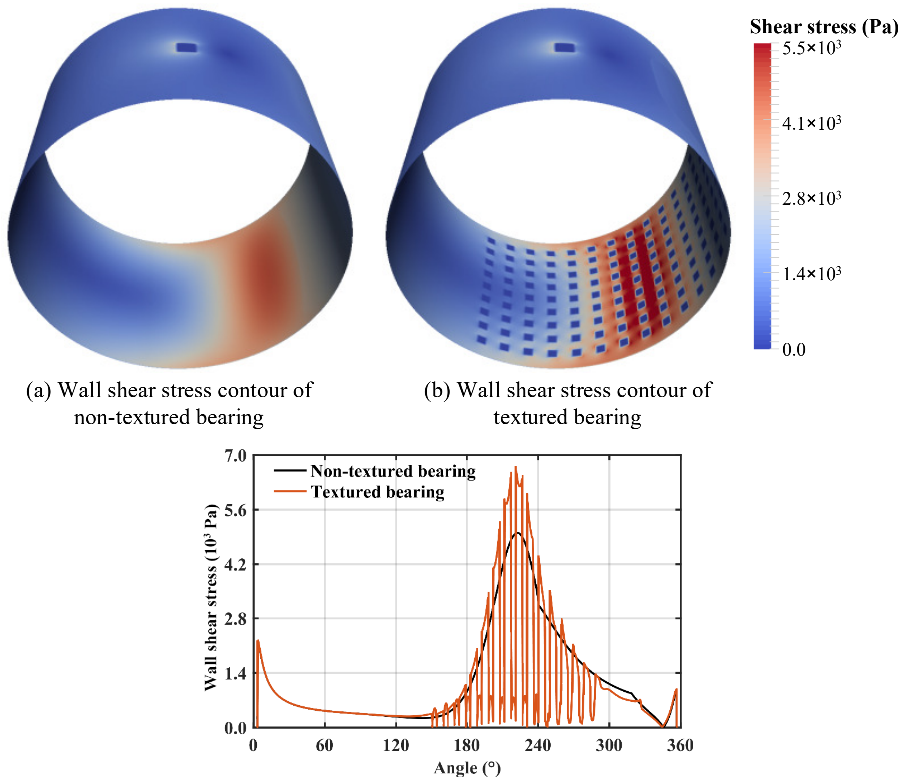

(a) Wall shear stress contour of non-textured bearing

(b) Wall shear stress contour of textured bearing

(c) Wall shear stress profiles along the center plane of non-textured and textured bearings

Fig. 6 Comparison of wall shear stress distributions of non-textured and textured bearings.

Table 4 Design range with minimum and maximum values of input parameters

Parameter	Minimum value	Maximum value
Textured width ratio, w_t/W	0.2	0.96
Texture depth ratio, d_t/C	0	3
Starting angle of textured zone, α (°)	5	180
Coverage of texture zone, cov (°)	0	170
External load, F (N)	100	450

Table 5 Design parameters for the initial ANN model

Parameter	Specification
Training algorithm	Levenberg–Marquardt algorithm
Number of hidden layers	1
Number of neurons in hidden layer	5
Activation function for hidden layer	tanh
Activation function for output layer	Purelin
Learning rate	10^{-2}
Division of data	Random
Data division	70%—Training 15%—Validation 15%—Test

machine from classification problem to regression task. The main concept is to find a hyperplane that best represents the relationship between the input features and the target variable. Therefore, an optimization is conducted to minimize the error between predicted and target values. The final prediction function $f(x)$ in SVR is constructed from the support vectors as Eq. (9) shows

$$f(x)=\sum_{i=1}^{n}(\alpha_i-\alpha_i^*)K(x,x_i)+b \tag{9}$$

where α_i and α_i^* are the support vectors; $K(x,x_i)$ is the kernel function; b is the bias.

During this process, the kernel function is applied to map the input data to a higher dimensional space, which is essential for the prediction accuracy [59]. To comprehensively evaluate the prediction accuracy, five commonly used kernel functions in SVR are compared: the linear polynomial kernel, the quadratic polynomial kernel, the cubic polynomial kernel, the medium Gaussian kernel (with a kernel size of 2.2), and the coarse Gaussian kernel (with a kernel size of 8.9) [60].

3.2.3 *Gaussian process regression*

The GPR method is one of the non-parametric Bayesian methods. GPR defines the distribution over functions, which are typically assumed to be Gaussian. It is characterized by two functions: mean function $m(x)$ and kernel function $C(x,x')$, as Eq. (10) shows [61]. With the prior predictive distribution and the training set, the posterior distribution over functions can be obtained by constraining the prior joint distribution [62]. In this work, four commonly used kernel functions in the GPR model are considered for comparison, including the squared exponential kernel, the Matern 5/2 kernel, the exponential kernel, and the rational quadratic kernel [60]:

$$g(x)\sim \mathrm{GP}\left(m(x),C(x,x')\right) \tag{10}$$

where $x,x'\in X$, and X denotes the space of input points.

3.2.4 *Performance evaluation*

To evaluate the prediction performance of the ML models, the mean square error (MSE) and the correlation coefficient (R) are calculated. MSE, defined in Eq. (11), is a measure of the average squared difference between the predicted and target values.

$$\mathrm{MSE}=\frac{1}{N}\sum_{i=1}^{N}(y_i-\hat{y}_i)^2 \tag{11}$$

where y_i represents the target value, and $\hat{y}_i$ represents the predicted value from the ML models. A lower MSE value indicates a better estimation performance, while a higher MSE value indicates a poorer estimation performance.

The correlation coefficient (R), defined in Eq. (12), provides information about the correlation between the predicted and target values.

$$R=\frac{\sum_{i=1}^{N}(y_i-\bar{y}_i)(\hat{y}_i-\bar{\hat{y}}_i)}{\sqrt{\sum_{i=1}^{N}(y_i-\bar{y}_i)^2\sum_{i=1}^{N}(\hat{y}_i-\bar{\hat{y}}_i)^2}} \tag{12}$$

where $\bar{y}_i$ and $\bar{\hat{y}}_i$ are the mean target and predicted values, respectively. A high R value close to 1 indicates a strong relationship between the predicted and target values. Conversely, an R value of 0 suggests a random connection or no correlation between the predicted and target values [63].

3.3 Comparison of different machine learning methods

To determine the most appropriate prediction method for textured journal bearings, the above-mentioned three different ML methods are trained based on identical data sets. The prediction performance of each ML method is illustrated by comparing their respective R_{test} and $\mathrm{MSE}_{\text{test}}$ values in Fig. 7. The results of the SVR models indicate that, the cubic polynomial kernel function shows the best prediction accuracy, with the R_{test} value of 0.91 and the $\mathrm{MSE}_{\text{test}}$ value of 2.86×10^{-3}. For the GPR models, the exponential kernel function shows the best prediction accuracy, with the R_{test} value of 0.92 and the $\mathrm{MSE}_{\text{test}}$ value of 2.16×10^{-3}. Despite utilizing the preliminary structure, the ANN model exhibits the R_{test} value of 0.95, which is higher than the corresponding values of the SVR and GPR models. Furthermore, the ANN model achieves a lower $\mathrm{MSE}_{\text{test}}$ value of 1.99×10^{-3} compared to the SVR and GPR models. Overall, the GPR models exhibit superior prediction accuracy compared to the SVR models. In addition, the ANN model achieves higher prediction accuracy than both the GPR and SVR models under the current hyperparameters. This conclusion is similar to the findings drawn in the study by Tošić et al. [64] that the ANN model showed the best performance in their tribological application.

Therefore, as the most promising method among three ML methods examined in this work, the ANN method is selected for the friction prediction of textured journal bearings. More detailed regression results of the ANN model are shown in Fig. 8. It can be observed that, the R values for the training, validation, test, and overall data sets are 0.965, 0.954, 0.946, and 0.957, respectively.

Furthermore, to more straightforwardly evaluate the prediction accuracy of the trained ANN model, the friction forces of 20 evaluation data sets are predicted. The predicted results are then compared with the true results from the aforementioned CFD model. The comparison results, along with the errors between the predicted and true values, are depicted in Fig. 9. It can be found that the overall trend of the predicted values by the ANN model is consistent with the true values. The average prediction accuracy stands at 95.89%. However, as observed from Fig. 9(b), it is evident that certain significant errors are identifiable, with a maximum deviation of 13.17%.

To analyze the reasons behind the high deviation, the operating conditions and texture parameters of the 10th and 15th data sets are analyzed. A possible reason for the significant error in the 10th data set is that, this data set corresponds to the case where textures are distributed at the minimum oil film region. In this context, textures can effectively reduce the friction force of journal bearings [14]. It may be due to that the neural network with current architecture is not able to accurately predict this complex relationship under this specific condition. Therefore, the friction predicted by the ANN model shows deviation from the true value. The 15th data set has a similar condition, with textures distributed at the minimum oil film region. This indicates the necessity for further optimization of the prediction accuracy of the surrogate model.

4 Optimization of the surrogate model

With the identical data sets, the accuracy of the ANN model depends on the network architecture [65], as well as the appropriate initial weights and biases for each neuron [66]. To improve the prediction accuracy of the ANN model based on the current data sets, the ANN model is optimized through the cross-validation-based hyperparameter optimization and the genetic algorithm. The cross-validation (CV) method is used to evaluate various architecture parameter combinations, which helps to identify an optimal neural network architecture. Subsequently, the genetic algorithm (GA) is utilized for searching the appropriate initial weights and biases for each neuron.

4.1 Optimization of the ANN architecture through cross-validation

The CV method is a robust technique for model evaluation and

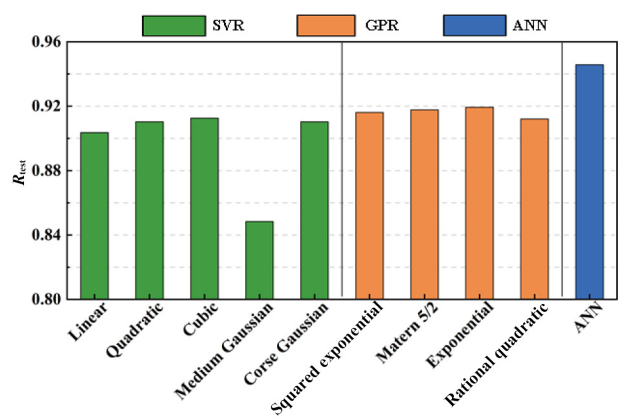

(a) R_{test} values of SVR, GPR, and ANN models

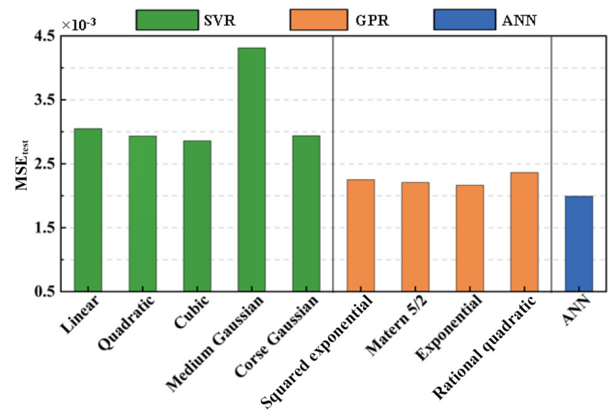

(b) $\mathrm{MSE}_{\text{test}}$ values of SVR, GPR, and ANN models

Fig. 7 Prediction performance of SVR, GPR, and ANN models.

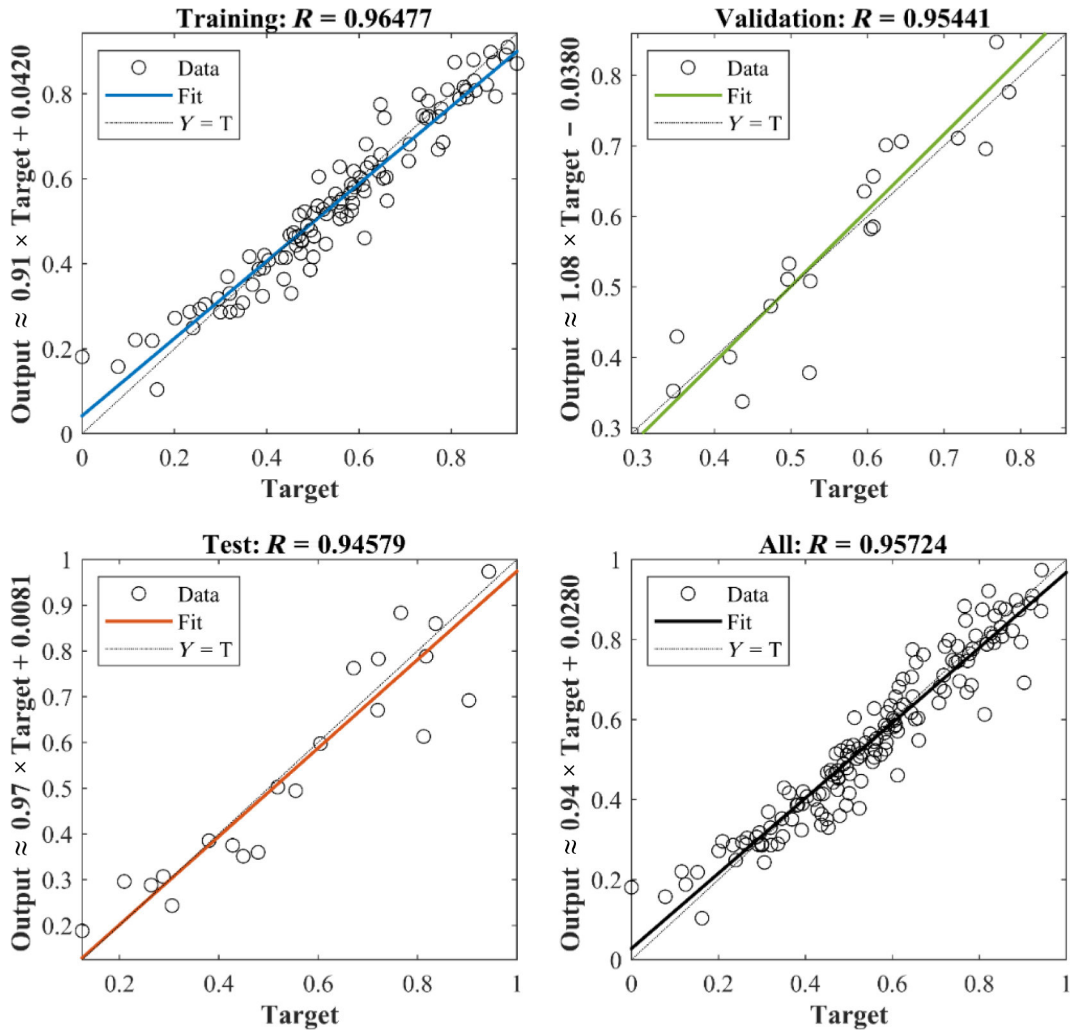

Fig. 8 *R* values for training, validation, test, and overall data sets for the initial ANN model (*Y* represents the *y*-axis value, while *T* represents the target value).

hyperparameter optimization in the field of artificial neural networks. In this work, the architecture hyperparameters of the ANN model is optimized through the widely-used *k*-fold cross-validation, as shown in Fig. 10 [67]. The data sets are split into *k* subsets of approximately equal size. The model is trained *k* rounds. For each round *i* (1 to *k*), *k*−1 folds are used for training and the remaining fold is for testing. This process ensures that every data point is used for both training and testing exactly once. Therefore, it ensures the high reliability and generalizability. To evaluate the overall performance of the ANN model with different architectures, the MSE value on the test fold is calculated across all iterations. The average performance is obtained by Eq. (13). In the present study, 5-fold cross-validation is used

$$\mathrm{MSE}_{\mathrm{avg}}=\frac{1}{k}\sum_{i=1}^{k}\mathrm{MSE}_i \tag{13}$$

where $\mathrm{MSE}_{\mathrm{avg}}$ is the average MSE value for all iterations, and MSE_i is the MSE value for each iteration.

In this work, four key architecture parameters of the ANN model are selected: the number of hidden layers, the number of neurons in each hidden layer, the learning rate of the ANN model, and the type of activation function in hidden layers [68]. The optimization range of each parameter is shown in Table 6. Then, the optimization process for the architecture parameters is conducted through the following steps:

Step 1: The optimization range for the four architecture parameters is defined as Table 6 shows.

Step 2: Based on the optimization range, the four architecture parameters are fully combined using nested loops. In this work, 4,275 groups of combinations are generated.

Step 3: Each combination undergoes 5-fold cross-validation. The MSE value of each combination is evaluated on the 5 different test folds, respectively.

Step 4: The average MSE value ($\mathrm{MSE}_{\mathrm{avg}}$) for each combination is recorded and compared. The best parameter combination with the minimum ($\mathrm{MSE}_{\mathrm{avg}}$) is identified at the end.

Step 5: The optimal parameter combination is outputted, and therefore the optimal ANN architecture is determined.

After the architecture optimization through the above process, the selected number of hidden layers is 2. The number of neurons in each hidden layer is 12 and 4. The learning rate is 10^{-2} and the activation function in hidden layers is ReLU. The *R* values for the ANN model with the determined architecture by CV (shortly CV-ANN) are depicted in Fig. 11. The prediction performance shows a notable improvement, with the *R* value for all data sets increasing from 0.957 to 0.974. In addition, the R_{test} value increases from 0.946 to 0.969, and the $\mathrm{MSE}_{\mathrm{test}}$ value is reduced from 1.99×10^{-3} to 1.45×10^{-3}, which also indicates the better prediction performance than the initial ANN model.

Based on 20 evaluation data sets, Fig. 12 depicts a more straightforward comparison between the true values and predicted

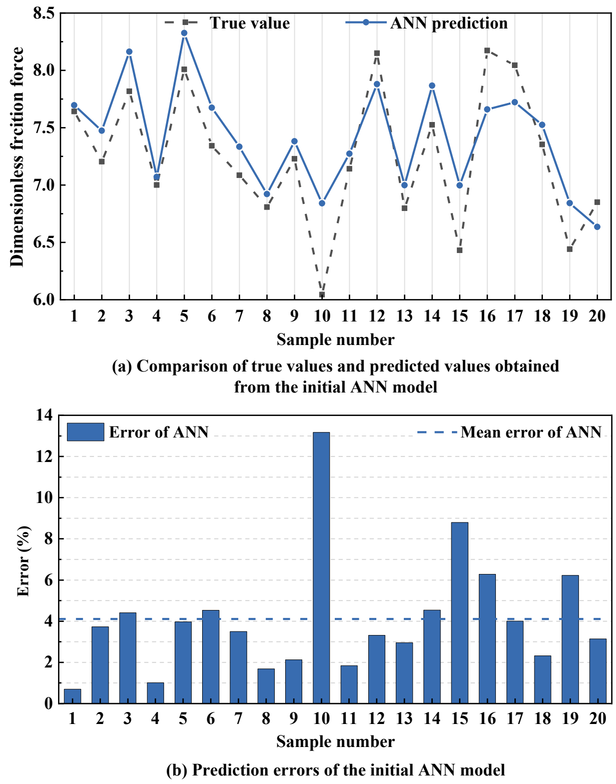

Fig. 9 Prediction performance of the initial ANN model.

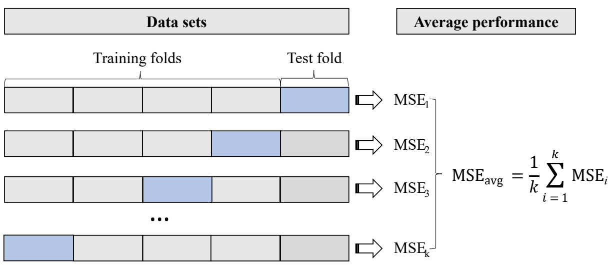

Fig. 10 Process of k-fold cross-validation.

Table 6 Optimization range of architecture parameters for the ANN model

Parameter	Range
Number of hidden layers	1–3
Number of neurons in hidden layer	2–20
Learning rate	10^{-5}–10^{-1}
Activation function on hidden layers	tanh, sigmoid, ReLU

values from the ANN and CV-ANN models. Compared to the initial ANN model, the CV-ANN model exhibits higher accuracy in predicting the friction force of textured journal bearings. In terms of average prediction accuracy, it increases from 95.89% to 97.82%. Notably, the prediction error can be consistently kept below 6% for each data set. Especially for the 10^{th} data set, the prediction error is reduced from 13.17% to 5.29%. Meanwhile, the prediction error for the 15^{th} data set decreases from 8.80% to 2.09%. This suggests that the new architecture of the ANN model can further capture the complex relationship between the textured parameters and the bearing friction. The improved prediction accuracy verifies the importance of the architecture parameters on the prediction accuracy of the ANN model, which was also demonstrated in Refs. [58, 69]. However, compared with the optimal architecture results in previous studies [58, 69], it can be seen that the suitable architecture is dependent on the specific applications and data sets. The CV-based hyperparameter optimization introduced above offers a comprehensive way to determine the suitable architecture parameters according to different applications and data sets.

4.2 Optimization of the prediction performance through genetic algorithm

In addition to the architecture parameters, the initial weights and biases also have a considerable impact on the prediction accuracy of the ANN model [66, 70]. To further improve the prediction accuracy, the GA is used to determine the optimal initial weights and biases based on the CV-ANN model. The GA is derived from the principle of natural selection and population genetics. During the process of the GA, optimization parameters are incorporated into a population of encoded individuals, which are selected, crossed over, and mutated based on a fitness function [71]. The optimization process of the GA in this work is shown in Fig. 13 [72].

The process starts from initializing the GA parameters, including the population size (S), the crossover probability (P_c), the mutation probability (P_m), the generation size (G_s), and the maximum stalled generations (S_{max}). The values of these parameters are listed in Table 7. In the next step, the fitness value of each individual in the population is evaluated with the fitness function presented in Eq. (14). Minimization of the fitness value is the goal of the optimization. In the current study, the fitness value refers to the difference between 1 and the R values for training, validation, test, and overall datasets:

$$\mathrm{fit}(x) = \sum_{i=1}^{4} |R_i(x) - 1| \tag{14}$$

where $R_i(x)$ represents the R value under the individual x, and the indices i = 1, 2, 3, 4 refer to training, validation, test, and overall data sets, respectively; x is the initial weights and biases of the neural network:

$$x = [\boldsymbol{w}_{\mathrm{in},1}, \boldsymbol{B}_1, \boldsymbol{w}_{1,2}, \boldsymbol{B}_2, \boldsymbol{w}_{2,\mathrm{out}}, \boldsymbol{B}_{\mathrm{out}}] \tag{15}$$

where $\boldsymbol{w}_{\mathrm{in},1}, \boldsymbol{w}_{1,2}$, and $\boldsymbol{w}_{2,\mathrm{out}}$ represent the weight matrices from the input layer to the first hidden layer, from the first hidden layer to the second hidden layer, and from the second hidden layer to the output layer, respectively; $\boldsymbol{B}_1, \boldsymbol{B}_2$, and $\boldsymbol{B}_{\mathrm{out}}$ represent the bias vectors of the first hidden layer, the second hidden layer, and the output layer, respectively.

The termination criteria for the optimization are either reaching the maximum generation size or no improvement in the best fitness value over the maximum number of stalled generations. If the criteria cannot be met in the current population, the mating will be initiated to recombine parent population and create offspring through selection, crossover, and mutation. Subsequently, a new population is generated and will be evaluated repeatedly until the termination criteria are achieved. Eventually, after the optimization through the GA, the optimal initial weights and biases for each neuron are determined and utilized in the training process of the ANN model.

Through the joint optimization using the CV and GA methods, both the neural network architecture as well as the initial weights and biases are optimized. The prediction performance of the optimized ANN model (shortly GA-CV-ANN) is shown in Fig. 14. The R values for training, validation, test, and overall data sets are improved. Eventually, compared to the initial ANN model, the R values for the training, validation, test, and overall data sets are significantly improved from 0.965 to 0.991, from 0.954 to 0.984, from 0.946 to 0.977, and from 0.957 to 0.988, respectively. The

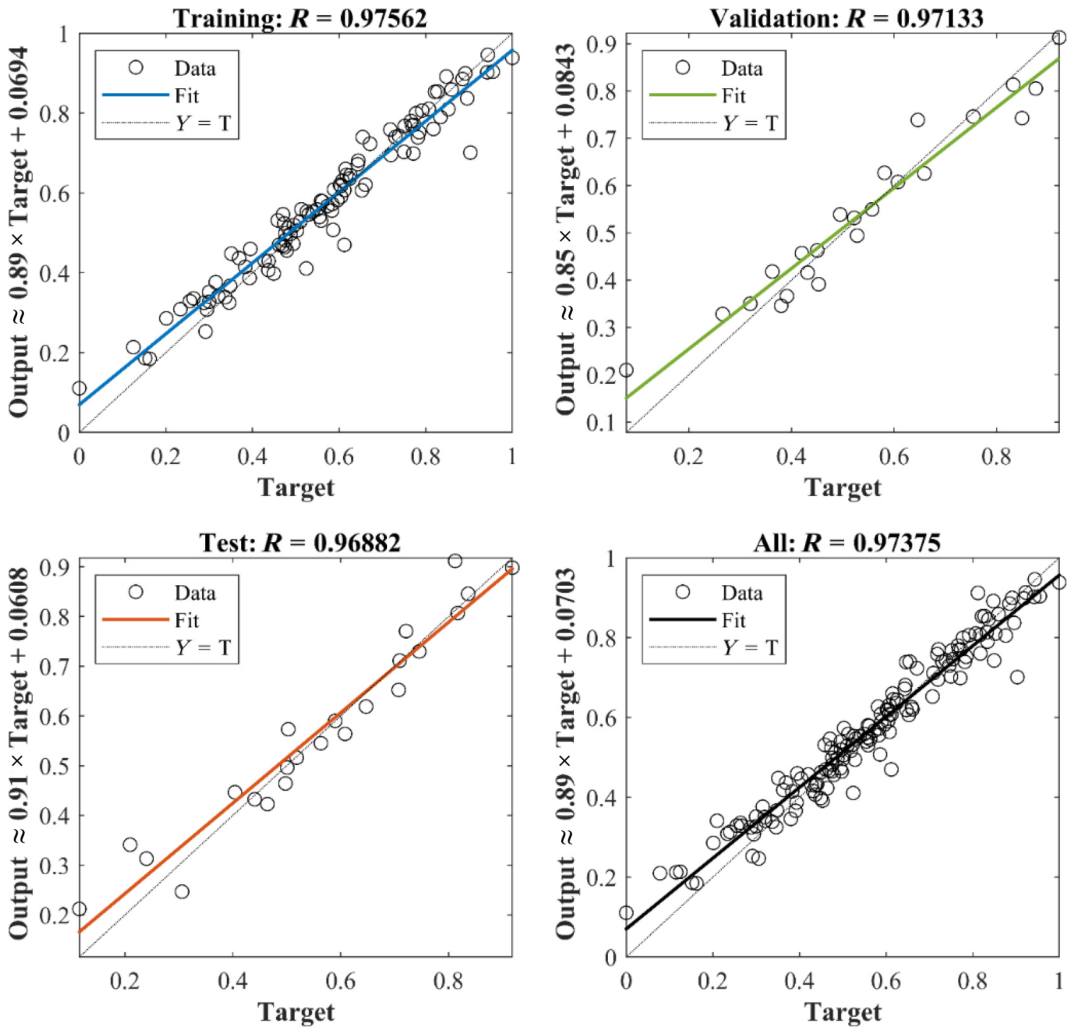

Fig. 11 R values for the training, validation, test, and overall data sets for CV-ANN model (Y represents the y-axis value, while T represents the target value).

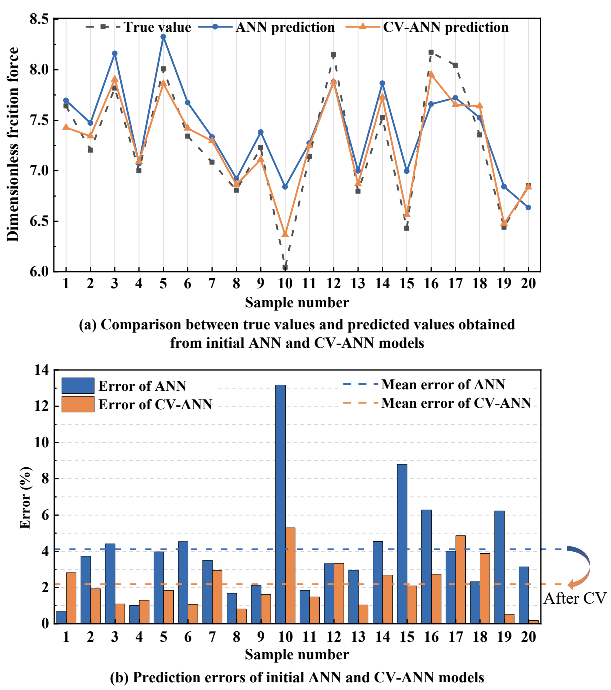

Fig. 12 Prediction performance of initial ANN and CV-ANN models.

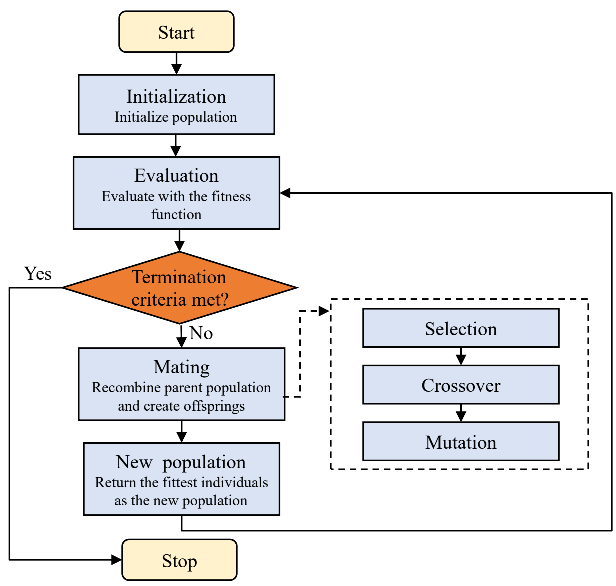

Fig. 13 Optimization process of GA model.

Table 7 Parameters of the GA model

Parameter	Value	Parameter	Value
Population size, S	150	Selection function	Tournament selection
Crossover probability, P_c	0.8	Crossover function	Two-point crossover
Mutation probability, P_m	0.15	Mutation function	Gaussian mutation
Generation size, G_s	150	—	—
Maximum stalled generations, S_{max}	50	—	—

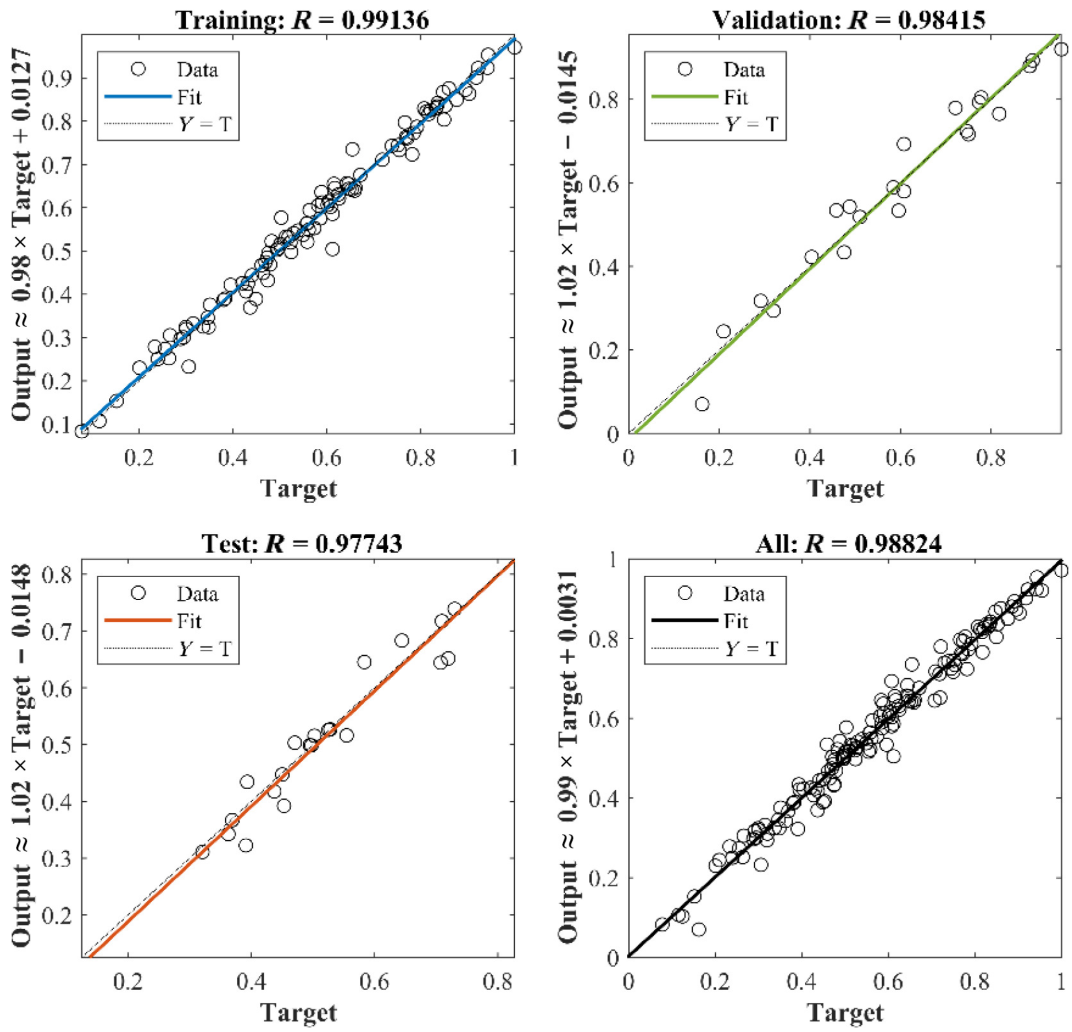

Fig. 14 R values for the training, validation, test, and overall data sets for GA-CV-ANN model (Y represents the y-axis value, while T represents the target value).

MSE_{test} value is decreased from 1.99×10^{-3} to 1.19×10^{-3}, which also indicates the improved prediction performance of the ANN model.

Meanwhile, the prediction accuracy of the GA-CV-ANN model is also further enhanced compared with the CV-ANN model. It can be seen from Fig. 15(a) that, after the further optimization through GA, the predicted values of the ANN model are overall closer to the true values. From the comparison of the error values (Fig. 15(b)), the overall prediction accuracy reaches 98.81%. Only one set of data has an error of 3.25%, which is also the maximum error. All other errors are below 3%. Half of the evaluation data sets can be predicted with an error of less than 1%. Compared to the initial ANN model, its capability to capture the complex relationship between texture parameters and the bearing friction is now enhanced. This can be observed by the reduced prediction errors for the 10th and 15th data sets, where textures are distributed at the minimum oil film region. The prediction errors for these two data sets are reduced from 13.17% to 1.46% and from 8.80% to 3.25%.

After the combined optimization through the CV-based hyperparameter optimization and the GA, the prediction accuracy of the ANN model has significantly improved. The proposed optimization method shows a promising way to improve the prediction accuracy of the ANN model under identical data sets. This is interesting for the application with limited data sets, particularly for the training data of high-fidelity CFD simulations that are expensive in terms of simulation time.

5 Conclusions

Surface textures have gained notable attention due to its reduction on the friction of journal bearings. To accurately predict the friction performance of textured journal bearings, the

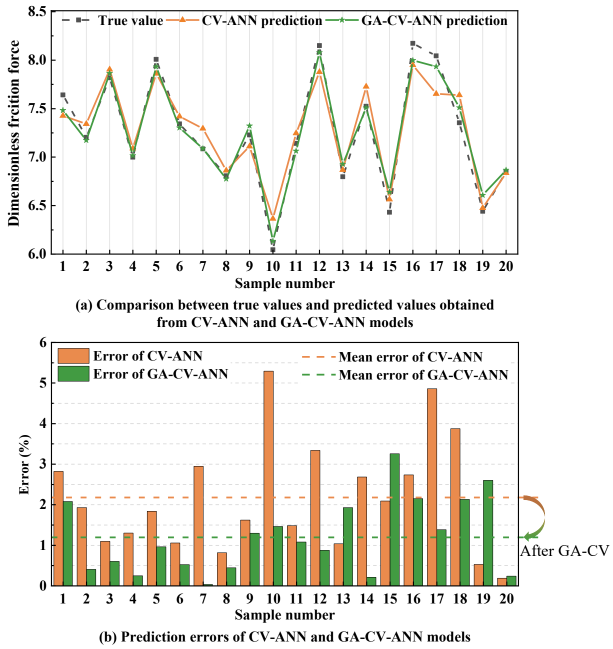

Fig. 15 Prediction performance of CV-ANN and GA-CV-ANN models.

computational fluid dynamics (CFD) models employing a dynamic mesh algorithm are built up. Subsequently, data sets generated from CFD simulations are used to develop ML-based surrogate models. Three machine learning (ML) methods are compared in this study to select a suitable prediction algorithm. Considering the high computational cost of CFD simulations, the prediction accuracy of the surrogate model is enhanced with identical data sets. The findings can be summarized as follows:

(1) The proposed CFD model combined with a dynamic mesh algorithm can describe the flow field and predict the friction performance for textured journal bearings. The simulation results are in a good agreement with experimental results.

(2) In this work, the artificial neural network (ANN) model shows the best prediction performance on the friction prediction of textured journal bearings, compared with the support vector regression (SVR) and Gaussian process regression (GPR) models.

(3) Through the hyperparameter optimization based on cross-validation (CV), the appropriate ANN architecture is determined. Using the optimized ANN architecture, the overall prediction accuracy is enhanced from 95.89% to 97.82%. The maximum prediction error for each data set is decreased from 13.17% to 5.29%.

(4) After the further optimization through genetic algorithm (GA), the prediction accuracy of the ANN model has been further improved. The overall prediction accuracy is risen to 98.81%. The maximum prediction error for each data set is decreased to 3.25%, with the average error of 1.19%.

The findings in this work can provide a promising approach to build up a highly efficient and accurate surrogate model based on machine learning, particularly in cases with limited available data sets. For future work, the developed surrogate model can be utilized for the optimization design of surface textures in journal bearings.

Appendix

In this work, the cavitation effect is considered using the homogeneous equilibrium model, which assumes the mixture of liquid and vapor to be in a mechanical and thermodynamic equilibrium [50]. To consider the compressibility of the mixture flow, the cavitation model is based on the relations of the pressure and density as a closure equation, which is employed by Eq. (A1) [50]:

$$\frac{\mathrm{D}\rho_{\mathrm{m}}}{\mathrm{D}t}=\Psi_{\mathrm{m}}\frac{\mathrm{D}p}{\mathrm{D}t} \tag{A1}$$

where ρ_{m} is the density of the mixture of oil and vapour; Ψ_{m} is the compressibility coefficient of the mixture; p is the pressure.

Then, the mass fraction of vapor γ is calculated by Eq. (A2) [50]:

$$\gamma=\frac{\rho_{\mathrm{m}}-\rho_{\mathrm{l,sat}}}{\rho_{\mathrm{v,sat}}-\rho_{\mathrm{l,sat}}} \tag{A2}$$

where $\rho_{\mathrm{l,sat}}$ and $\rho_{\mathrm{v,sat}}$ are density of the liquid and vapor at saturation pressure, respectively.

Afterwards, the mixture compressibility Ψ_{m} obtained by the Wallis linear model [73] and the local mixture viscosity η_{m} are computed by

$$\Psi_{\mathrm{m}}=\gamma\Psi_{\mathrm{v}}+(1-\gamma)\,\Psi_{\mathrm{l}} \tag{A3}$$

$$\eta_{\mathrm{m}}=\gamma\eta_{\mathrm{v}}+(1-\gamma)\,\eta_{\mathrm{l}} \tag{A4}$$

where Ψ_{l} and Ψ_{v} are the compressibilities of liquid and vapor respectively; η_{l} and η_{v} are the viscosities of liquid and vapor respectively.

Next, the mixture density ρ_{m} can be calculated by considering the fraction of vapor. The mixture's equilibrium equation of state is as Eq. (A5) [50]:

$$\rho_{\mathrm{m}}=(1-\gamma)\,\rho_{\mathrm{l}}^{0}+(\gamma\Psi_{\mathrm{v}}+(1-\gamma)\,\Psi_{\mathrm{l}})\,P_{\mathrm{sat}}+\Psi_{\mathrm{m}}(P-P_{\mathrm{sat}}) \tag{A5}$$

where ρ_{l}^{0} is the density of liquid at reference pressure; P_{sat} is the saturation pressure.

Combined with this cavitation model, the N–S equations, which are derived from mass conservation and momentum conservation, are used to solve the fluid flow [52]:

$$\frac{\partial}{\partial t}(\rho_{\mathrm{m}})+\nabla\cdot(\rho_{\mathrm{m}}\boldsymbol{v}_{\mathrm{m}})=0 \tag{A6}$$

$$\frac{\partial}{\partial t}(\rho_{\mathrm{m}}\boldsymbol{v}_{\mathrm{m}})+\nabla\cdot(\rho_{\mathrm{m}}\boldsymbol{v}_{\mathrm{m}}\boldsymbol{v}_{\mathrm{m}})-\nabla\cdot(\bar{\bar{\tau}})=-\nabla p+S_{\mathrm{v}} \tag{A7}$$

where $\boldsymbol{v}_{\mathrm{m}}$ is the velocity vector of the mixture; S_{v} is the gravity force.

In this work, the lubricant is assumed as a general Newtonian fluid, for which viscosity is independent of shear stress [52]. Under this condition, the shear stress term $\bar{\bar{\tau}}$ can be expressed in more detail as Eq. (A8):

$$\bar{\bar{\tau}}=\eta_{\mathrm{m}}\left[\nabla\boldsymbol{v}_{\mathrm{m}}+(\nabla\boldsymbol{v}_{\mathrm{m}})^{T}\right]+\frac{2}{3}\nabla\cdot\boldsymbol{v}_{\mathrm{m}}\cdot\bar{\bar{I}} \tag{A8}$$

where $\bar{\bar{I}}$ is the unit tensor, and the second term on the right-hand side is the effect of volume dilation.

Acknowledgements

The authors would like to thank the China Scholarship Council (No. CSC202106450023) and the Deutsche Forschungsgemeinschaft (DFG, German Research Foundation: 511282384) for supporting this work. Simulations were performed with computing resources granted by RWTH Aachen University under project ID rwth1399.

Declaration of competing interest

The authors have no competing interests to declare that are relevant to the content of this article. The author Georg Jacobs is the Editorial Board Member of this journal.

References

[1] König F, Sous C, Jacobs G. Numerical prediction of the frictional losses in sliding bearings during start-stop operation. *Friction* **9**(3): 583–597 (2021)

[2] Rosenkranz A, Grützmacher P G, Gachot C, Costa H L. Surface texturing in machine elements A critical discussion for rolling and sliding contacts. *Adv Eng Mater* **21**(8): 1900194 (2019)

[3] Holmberg K, Erdemir A. Influence of tribology on global energy consumption, costs and emissions. *Friction* **5**(3): 263–284 (2017)

[4] Nie T, Yang K, Zhou L, Wu X, Wang Y. CFD analysis of load capacity of journal bearing with surface texture. *Energy Rep* **8**: 327–334 (2022)

[5] Gropper D, Wang L, Harvey T J. Hydrodynamic lubrication of textured surfaces: A review of modeling techniques and key findings. *Tribol Int* **94**: 509–529 (2016)

[6] Meng Y G, Xu J, Jin Z M, Prakash B, Hu Y Z. A review of recent advances in tribology. *Friction* **8**(2): 221–300 (2020)

[7] Etsion I. State of the art in laser surface texturing. *J Tribol* **127**(1): 248–253 (2005)

[8] Gachot C, Grützmacher P, Rosenkranz A. Laser surface texturing of TiAl multilayer films: Effects of microstructure and topography on friction and wear. *Lubricants* **6**(2): 36 (2018)

[9] König F, Rosenkranz A, Grützmacher P G, Mücklich F, Jacobs G. Effect of single- and multi-scale surface patterns on the frictional performance of journal bearings–A numerical study. *Tribol Int* **143**: 106041 (2020)

[10] Profito F J, Vladescu S C, Reddyhoff T, Dini D. Numerical and experimental investigation of textured journal bearings for friction reduction. *Tribol Int* **195**: 109643 (2024)

[11] Adjemout M, Brunetière N, Bouyer J. Numerical analysis of the texture effect on the hydrodynamic performance of a mechanical seal. *Surf Topogr—Metrol* **4**(1): 014002 (2016)

[12] Gachot C, Rosenkranz A, Hsu S M, Costa H L. A critical assessment of surface texturing for friction and wear improvement. *Wear* **372**: 21–41 (2017)

[13] Liu C L, Guo F, Wong P, Li X M. Laser pattern-induced unidirectional lubricant flow for lubrication track replenishment. *Friction* **10**(8): 1234–1244 (2022)

[14] Wang Y, Jacobs G, König F, Zhang S, von Goeldel S. Investigation of microflow effects in textures on hydrodynamic performance of journal bearings using CFD simulations. *Lubricants* **11**(1): 20 (2023)

[15] Costa H L, Hutchings I M. Some innovative surface texturing techniques for tribological purposes. *P I Mech Eng J—J-Eng* **229**(4): 429–448 (2015)

[16] Brunetière N, Tournerie B. Numerical analysis of a surface-textured mechanical seal operating in mixed lubrication regime. *Tribol Int* **49**: 80–89 (2012)

[17] Sharma S, Jamwal G, Awasthi R K. Enhancement of steady state performance of hydrodynamic journal bearing using chevron-shaped surface texture. *P I Mech Eng J—J-Eng* **233**(12): 1833–1843 (2019)

[18] Tala-Ighil N, Maspeyrot P, Fillon M, Bounif A. Effects of surface texture on journal-bearing characteristics under steady-state operating conditions. *P I Mech Eng J—J-Eng* **221**(6): 623–633 (2007)

[19] Dobrica M B, Fillon M, Pascovici M D, Cicone T. Optimizing surface texture for hydrodynamic lubricated contacts using a mass-conserving numerical approach. *P I Mech Eng J—J-Eng* **224**(8): 737–750 (2010)

[20] Tala-Ighil N, Fillon M, Maspeyrot P. Effect of textured area on the performances of a hydrodynamic journal bearing. *Tribol Int* **44**(3): 211–219 (2011)

[21] Khatri C B, Sharma S C. Influence of textured surface on the performance of non-recessed hybrid journal bearing operating with non-Newtonian lubricant. *Tribol Int* **95**: 221–235 (2016)

[22] Liang X X, Liu Z L, Wang H J, Zhou X H, Zhou X C. Hydrodynamic lubrication of partial textured sliding journal bearing based on three-dimensional CFD. *Ind Lubr Tribol* **68**(1): 106–115 (2016)

[23] Brizmer V, Kligerman Y. A laser surface textured journal bearing. *J Tribol* **134**(3): 031702 (2012)

[24] Cupillard S, Cervantes M, Glavatskih S. A CFD study of a finite textured journal bearing. In: Proceedings of the 24th IAHR Symposium on Hydraulic Machinery and Systems, Foz do Iguassu, Brazil, 2008.

[25] Cupillard S, Glavatskih S, Cervantes M J. Computational fluid dynamics analysis of a journal bearing with surface texturing. *P I Mech Eng J—J-Eng* **222**(2): 97–107 (2008)

[26] Lin Q Y, Bao Q K, Li K J, Khonsari M M, Zhao H. An investigation into the transient behavior of journal bearing with surface texture based on fluid-structure interaction approach. *Tribol Int* **118**: 246–255 (2018)

[27] Marian M, Almqvist A, Rosenkranz A, Fillon M. Numerical micro-texture optimization for lubricated contacts—A critical discussion. *Friction* **10**(11): 1772–1809 (2022)

[28] Singh N, Awasthi R K. Theoretical investigation of surface texture effects on the performance characteristics of hydrodynamic two-lobe journal bearing. *P I Mech Eng J—J-Eng* **234**(11): 1712–1725 (2020)

[29] Marian M, Tremmel S. Current trends and applications of machine learning in tribology—A review. *Lubricants* **9**(9): 86 (2021)

[30] König F, Wirsing F, Singh A, Jacobs G. Machine-learning-based wear prediction in journal bearings under start–stop conditions. *Lubricants* **12**(8): 290 (2024)

[31] Moschopoulos M, Rossopoulos G N, Papadopoulos C I. Journal bearing performance prediction using machine learning and octave-band signal analysis of sound and vibration measurements. *Pol Marit Res* **28**(3): 137–149 (2021)

[32] Hess N, Shang L Z. Machine learning prediction of journal bearing pressure distributions, considering elastic deformation and cavitation. In: Proceedings of ASME/BATH 2021 Symposium on Fluid Power and Motion Control, Virtual, Online, 2021: FPMC2021-68483.

[33] Roy B, Dey S. Machine learning-based performance analysis of two-axial-groove hydrodynamic journal bearings. *P I Mech Eng J—J-Eng* **235**(10): 2211–2224 (2021)

[34] Baş H S, Karabacak Y E. Machine learning-based prediction of friction torque and friction coefficient in statically loaded radial journal bearings. *Tribol Int* **186**: 108592 (2023)

[35] Otero J E, Ochoa E D L G, Vallinot I B, Tanarro E C. Optimising the design of textured surfaces for reducing lubricated friction coefficient. *Lubr Sci* **29**(3): 183–199 (2017)

[36] Marian M, Grützmacher P, Rosenkranz A, Tremmel S, Mücklich F, Wartzack S. Designing surface textures for EHL point-contacts—Transient 3D simulations, meta-modeling and experimental validation. *Tribol Int* **137**: 152–163 (2019)

[37] Li Z S, Li J Q, An B, Li R. The design method for surface texture of sliding friction pairs based on machine learning under mixed lubrication. *Tribol Int* **194**: 109563 (2024)

[38] Mohammed S, Budach L, Feuerpfeil M, Ihde N, Nathansen A, Noack N, Patzlaff H, Naumann F, Harmouch H. The effects of data quality on machine learning performance. *arXiv preprint* arXiv:2207.14529 (2022)

[39] Chen H H, Chen J P, Ding J H. Data evaluation and enhancement for quality improvement of machine learning. *IEEE Trans Reliab* **70**(2): 831–847 (2021)

[40] Wen S Z, Huang P. *Principles of Tribology*. Beijing (China): Tsinghua University Press, 2017.

[41] Arghir M, Roucou N, Helene M, Frene J. Theoretical analysis of the incompressible laminar flow in a macro-roughness cell. *J Tribol* **125** (2): 309–318 (2003)

[42] Keller D, Jacobs G, Neumann S. Development of a low-friction radial shaft seal: Using CFD simulations to optimise the microstructured sealing lip. *Lubricants* **8**(4): 41 (2020)
[43] Sahlin F, Glavatskih S B, Almqvist T, Larsson R. Two-dimensional CFD-analysis of micro-patterned surfaces in hydrodynamic lubrication. *J Tribo* **127**(1): 96–102 (2005)
[44] Wang W, He Y Y, Zhao J, Li Y, Luo J B. Numerical optimization of the groove texture bottom profile for thrust bearings. *Tribol Int* **109**: 69–77 (2017)
[45] Wang W, He Y Y, Li Y, Wei B, Hu Y T, Luo J B. Investigation on inner flow field characteristics of groove textures in fully lubricated thrust bearings. *Ind Lubr Tribol* **70**(4): 754–763 (2018)
[46] Xie Z, Li J, Tian Y, Du P, Zhao B, Xu F. Theoretical and experimental study on influences of surface texture on lubrication performance of a novel bearing. *Tribol Int* **193**: 109351 (2024)
[47] Xie Z L, Zhang Y, Zhou J Z, Zhu W D. Theoretical and experimental research on the micro interface lubrication regime of water lubricated bearing. *Mech Syst Signal Pr* **151**: 107422 (2021)
[48] Wang Y, Jacobs G, Zhang S, Klinghart B, König F. Lubrication mechanism analysis of textures in journal bearings using CFD simulations. *Ind Lubr Tribol* 77(1): 2–14 (2025)
[49] Sawicki J T, Rao T V V L N. Cavitation effects on the stability of a submerged journal bearing. *Int J Rotating Mach* **10**(3): 227–232 (2004)
[50] Feldermann A, Neumann S, Jacobs G. CFD simulation of elastohydrodynamic lubrication problems with reduced order models for fluid–structure interaction. *Tribol—Mater Surf In* **11**(1): 30–38 (2017)
[51] Lee D. Exploring elastohydrodynamic lubrication using finite-volume computational modelling techniques. Ph.D. Thesis. London (UK): Imperial College London, 2018.
[52] Greenshields C J, Weller H G. *Note on Computational Fluid Dynamics: General Principles*. Reading (UK): CFD Direct Limited, 2022.
[53] Gertzos K P, Nikolakopoulos P G, Papadopoulos C A. CFD analysis of journal bearing hydrodynamic lubrication by Bingham lubricant. *Tribol Int* **41**(12): 1190–1204 (2008)
[54] Moukalled F, Mangani L, Darwish M. *The Finite Volume Method in Computational Fluid Dynamics: An Advanced Introduction with OpenFOAM® and Matlab*. Berlin (Germany): Springer, 2016.
[55] Gupta K K, Kumar R, Kumar H, Sharma M. Study on effect of surface texture on the performance of hydrodynamic journal bearing. *Int J Eng Adv Technol* **3**(1): 49–54 (2013)
[56] Wang S H, Zheng J H, Wu X Y. Influence of surface texture configuration and depth on tribological performance of hydrodynamic journal bearing. *Appl Mech Mater* **155–156**: 318–323 (2012)
[57] Walker J, Questa H, Raman A, Ahmed M, Mohammadpour M, Bewsher S R, Offner G. Application of tribological artificial neural networks in machine elements. *Tribol Lett* **71**(1): 3 (2022)
[58] Marian M, Mursak J, Bartz M, Profito F J, Rosenkranz A, Wartzack S. Predicting EHL film thickness parameters by machine learning approaches. *Friction* **11**(6): 992–1013 (2023)
[59] Asadi A, Bakhtiyari A N, Alarifi I M. Predictability evaluation of support vector regression methods for thermophysical properties, heat transfer performance, and pumping power estimation of MWCNT/ZnO–engine oil hybrid nanofluid. *Eng Comput* **37**(4): 3813–3823 (2021)
[60] Mathworks Matlab. Choose regression model options. Available at https://de.mathworks.com/help/stats/choose-regression-model-options.html#bvmwe_w
[61] Momeni E, Dowlatshahi M B, Omidinasab F, Maizir H, Armaghani D J. Gaussian process regression technique to estimate the pile bearing capacity. *Arab J Sci Eng* **45**(10): 8255–8267 (2020)
[62] Hong S, Zhou Z. Application of Gaussian process regression for bearing degradation assessment. In: Proceedings of the 6th International Conference on New Trends in Information Science, Service Science and Data Mining, 2012: 644–648.
[63] Ostasevicius V, Paleviciute I, Paulauskaite-Taraseviciene A, Jurenas V, Eidukynas D, Kizauskiene L. Comparative analysis of machine learning methods for predicting robotized incremental metal sheet forming force. *Sensors* **22**(1): 18 (2022)
[64] Tošić M, Marian M, Habchi W, Lohner T, Stahl K. Application of machine learning for film thickness prediction in elliptical EHL contact with varying entrainment angle. *Tribol Int* **199**: 109940 (2024)
[65] Benardos P G, Vosniakos G C. Optimizing feedforward artificial neural network architecture. *Eng Appl Artif Intell* **20**(3): 365–382 (2007)
[66] Chang Y T, Lin J, Shieh J S, Abbod M F. Optimization the initial weights of artificial neural networks via genetic algorithm applied to hip bone fracture prediction. *Adv Fuzzy Syst* **2012**: 951247 (2012)
[67] Pu Y Y, Apel D B, Wei C. Applying machine learning approaches to evaluating rockburst liability: A comparation of generative and discriminative models. *Pure Appl Geophys* **176**(10): 4503–4517 (2019)
[68] Abdolrasol M G M, Suhail Hussain S M, Ustun T S, Sarker M R, Hannan M A, Mohamed R, Ali J A, Mekhilef S, Milad A. Artificial neural networks based optimization techniques: A review. *Electronics* **10**(21): 2689 (2021)
[69] Singh A, Wolf M, Jacobs G, König F. Machine learning based surrogate modelling for the prediction of maximum contact temperature in EHL line contacts. *Tribol Int* **179**: 108166 (2023)
[70] Qiu M Y, Song Y. Predicting the direction of stock market index movement using an optimized artificial neural network model. *PLoS One* **11**(5): e0155133 (2016)
[71] Katoch S, Chauhan S S, Kumar V. A review on genetic algorithm: Past, present, and future. *Multimed Tools Appl* **80**(5): 8091–8126 (2021)
[72] Boga C, Koroglu T. Proper estimation of surface roughness using hybrid intelligence based on artificial neural network and genetic algorithm. *J Manuf Process* **70**: 560–569 (2021)
[73] Wallis G B. *One-dimensional Two-phase Flow*. Mineola (USA): Dover Publications, 2020.

Yujun Wang received her master degree (2021) in power engineering and engineering thermophysics from China University of Petroleum (East China). Currently, she is a Ph.D. candidate at the Institute for Machine Elements and Systems Engineering, RWTH Aachen University, Germany. Her research focuses on data-driven prediction and optimization of textured journal bearings.